

# Packing of inhibitor molecules during area-selective atomic layer deposition studied using random sequential adsorption simulations

**Citation for published version (APA):**

Li, J., Tezsevin, I., Merckx, M. J. M., Maas, J. F. W., Kessels, W. M. M., Sandoval, T. E., & Mackus, A. J. M. (2022). Packing of inhibitor molecules during area-selective atomic layer deposition studied using random sequential adsorption simulations. *Journal of Vacuum Science and Technology A*, 40(6), Article 062409. <https://doi.org/10.1116/6.0002096>

**Document license:**  
TAVERNE

**DOI:**  
[10.1116/6.0002096](https://doi.org/10.1116/6.0002096)

**Document status and date:**  
Published: 01/12/2022

**Document Version:**  
Publisher's PDF, also known as Version of Record (includes final page, issue and volume numbers)

**Please check the document version of this publication:**

- A submitted manuscript is the version of the article upon submission and before peer-review. There can be important differences between the submitted version and the official published version of record. People interested in the research are advised to contact the author for the final version of the publication, or visit the DOI to the publisher's website.
- The final author version and the galley proof are versions of the publication after peer review.
- The final published version features the final layout of the paper including the volume, issue and page numbers.

[Link to publication](#)

**General rights**

Copyright and moral rights for the publications made accessible in the public portal are retained by the authors and/or other copyright owners and it is a condition of accessing publications that users recognise and abide by the legal requirements associated with these rights.

- Users may download and print one copy of any publication from the public portal for the purpose of private study or research.
- You may not further distribute the material or use it for any profit-making activity or commercial gain
- You may freely distribute the URL identifying the publication in the public portal.

If the publication is distributed under the terms of Article 25fa of the Dutch Copyright Act, indicated by the "Taverne" license above, please follow below link for the End User Agreement:

[www.tue.nl/taverne](http://www.tue.nl/taverne)

**Take down policy**

If you believe that this document breaches copyright please contact us at:

[openaccess@tue.nl](mailto:openaccess@tue.nl)

providing details and we will investigate your claim.

# Packing of inhibitor molecules during area-selective atomic layer deposition studied using random sequential adsorption simulations F

Cite as: J. Vac. Sci. Technol. A 40, 062409 (2022); <https://doi.org/10.1116/6.0002096>

Submitted: 20 July 2022 • Accepted: 10 October 2022 • Published Online: 10 November 2022

J. Li,  I. Tezsevin,  M. J. M. Merks, et al.

## COLLECTIONS

Paper published as part of the special topic on [Area Selective Deposition](#)

F This paper was selected as Featured



View Online





Export Citation



CrossMark








## Instruments for Advanced Science

- Knowledge,
- Experience,
- Expertise


Click to view our product catalogue

Contact Hiden Analytical for further details:  
[www.HidenAnalytical.com](http://www.HidenAnalytical.com)  
[info@hideninc.com](mailto:info@hideninc.com)




Gas Analysis

- ▶ dynamic measurement of reaction gas streams
- ▶ catalysis and thermal analysis
- ▶ molecular beam studies
- ▶ dissolved species probes
- ▶ fermentation, environmental and ecological studies




Surface Science

- ▶ UHVTPD
- ▶ SIMS
- ▶ end point detection in ion beam etch
- ▶ elemental imaging - surface mapping



Plasma Diagnostics

- ▶ plasma source characterization
- ▶ etch and deposition process reaction kinetic studies
- ▶ analysis of neutral and radical species



Vacuum Analysis

- ▶ partial pressure measurement and control of process gases
- ▶ reactive sputter process control
- ▶ vacuum diagnostics
- ▶ vacuum coating process monitoring

# Packing of inhibitor molecules during area-selective atomic layer deposition studied using random sequential adsorption simulations

F

Cite as: J. Vac. Sci. Technol. A 40, 062409 (2022); doi: 10.1116/6.0002096

Submitted: 20 July 2022 · Accepted: 10 October 2022 ·

Published Online: 10 November 2022

J. Li,<sup>1</sup> I. Tezsevin,<sup>1</sup> M. J. M. Merkx,<sup>1</sup> J. F. W. Maas,<sup>1</sup> W. M. M. Kessels,<sup>1</sup> T. E. Sandoval,<sup>2</sup> and A. J. M. Mackus<sup>1,a)</sup>

## AFFILIATIONS

<sup>1</sup>Department of Applied Physics, Eindhoven University of Technology 5600 MB, Eindhoven, The Netherlands<sup>2</sup>Department of Chemical and Environmental Engineering, Universidad Técnica Federico Santa María, Santiago, Chile**Note:** This paper is a part of the Special Topic Collection on Area Selective Deposition.<sup>a)</sup>**Author to whom correspondence should be addressed:** [A.J.M.Mackus@tue.nl](mailto:A.J.M.Mackus@tue.nl)

## ABSTRACT

Area-selective atomic layer deposition (ALD) is of interest for applications in self-aligned processing of nanoelectronics. Selective deposition is generally enabled by functionalization of the area where no growth is desired with inhibitor molecules. The packing of these inhibitor molecules, in terms of molecule arrangement and surface density, plays a vital role in deactivating the surface by blocking the precursor adsorption. In this work, we performed random sequential adsorption (RSA) simulations to investigate the packing of small molecule inhibitors (SMIs) on a surface in order to predict how effective the SMI blocks precursor adsorption. These simulations provide insight into how the packing of inhibitor molecules depends on the molecule size, molecule shape, and their ability to diffuse over the surface. Based on the RSA simulations, a statistical method was developed for analyzing the sizes of the gaps in between the adsorbed inhibitor molecules, serving as a quantitative parameter on the effectiveness of precursor blocking. This method was validated by experimental studies using several alcohol molecules as SMIs in an area-selective deposition process for SiO<sub>2</sub>. It is demonstrated that RSA simulations provide an insightful and straightforward method for screening SMIs in terms of their potential for area-selective ALD.

Published under an exclusive license by the AVS. <https://doi.org/10.1116/6.0002096>

## I. INTRODUCTION

The fabrication of devices with smaller feature sizes has been a main research topic in the semiconductor industry for the past few decades.<sup>1,2</sup> Devices based on 3D structures [e.g., FinFET, GAAFET (Gate-All-Around Field Effect Transistor)] have been and will be adopted to allow for further scaling.<sup>3,4</sup> Currently, semiconductor fabrication is based on top-down processing involving many sequential deposition, lithography, and etching steps.<sup>5,6</sup> The continued downscaling and the emerging of 3D device structures has put great demands on nanofabrication techniques.<sup>7,8</sup> It is becoming extremely challenging to meet the alignment criteria of features in multilayered structures, i.e., to sufficiently limit edge placement errors.<sup>9–11</sup>

Since the introduction of high-k dielectric materials in transistors,<sup>12</sup> atomic layer deposition (ALD) has emerged as an important technique for semiconductor manufacturing.<sup>13,14</sup> During an ALD process, precursor and co-reactant gases are alternately dosed on a substrate and participate in self-limiting surface reactions. ALD

offers the possibility to deposit thin films with excellent conformality over 3D nanostructures and accurate thickness control at the sub-nanometer level.<sup>15,16</sup> Since ALD is strongly dependent on the surface chemistry, the growth of a thin film can be controlled by modifying the chemical reactivity of the surface.<sup>17,18</sup> Area-selective deposition (ASD) involves the deposition of materials only on areas where it is desired and can thereby allow for self-aligned fabrication.<sup>19,20</sup> The starting point of ASD is a patterned substrate with surfaces where deposition is desired (i.e., the growth area), while deposition should be blocked on the other parts of the substrate (i.e., the non-growth area).

Area-selective ALD can be achieved by selectively modifying the surface to deactivate the surface for film growth.<sup>21–26</sup> Deactivation of the non-growth area has been demonstrated by surface functionalization using inhibitor molecules.<sup>27</sup> Much of the research in this field has been focused on using self-assembled monolayers (SAMs) to functionalize the surface before deposition.<sup>28–32</sup> SAMs are typically

formed in solution, whereas some recent studies also employed SAMs prepared via vapor-phase dosing.<sup>33,34</sup> However, as dimensions continue to shrink, even the use of SAMs could be limited for surface deactivation.<sup>35</sup> As an alternative, recent work explores the use of small molecule inhibitors (SMIs) to selectively functionalize the surface.<sup>36–38</sup> SMIs are small and volatile inhibitor molecules that can be dosed in the vapor phase during the ALD process, for example, in three-step (ABC-type) ALD cycles.<sup>38</sup> The use of SMIs is inspired on previous work by Yanguas-Gil *et al.* showing that alkyl alcohols, ketones, carboxylic acids, and  $\beta$ -diketones can be used to partially block the adsorption of precursor molecules, in order to reduce the growth rate of an ALD process.<sup>39</sup> In order to obtain ASD, in step A of an ABC-type cycle, the inhibitor molecules are supplied via vapor-phase dosing, and selectively adsorb on the non-growth area. Subsequently, in step B, the precursor molecules are dosed and are intended to be blocked on the non-growth area by the adsorbed inhibitor molecules, leading to selective precursor adsorption on the growth area. Finally, in step C, the coreactant is dosed to remove both the ligands of the precursor and the inhibitor molecules from the surface, which completes one ABC-type ALD cycle. The key merit of using SMIs lies in the vapor-phase dosing, making it compatible with industrial processing flows. In addition, by reapplying the inhibitor molecules every cycle, highly reactive coreactants such as ozone and plasma can be employed.<sup>40,41</sup> In our previous studies, acetylacetone (Hacac) was used as an inhibitor molecule for area-selective ALD of  $\text{SiO}_2$  and  $\text{WS}_2$ , which blocked the deposition on, for example,  $\text{Al}_2\text{O}_3$  as the non-growth area.<sup>37,38,42,43</sup> Furthermore, aniline was used to inhibit TiN ALD on Co and Ru, enabling area-selective TiN ALD on  $\text{SiO}_2$  and  $\text{Al}_2\text{O}_3$ .<sup>44</sup> Kim *et al.* used ethanethiol molecules for the deactivation of Co and Cu substrates to facilitate the area-selective deposition of  $\text{Al}_2\text{O}_3$  on  $\text{SiO}_2$  substrates.<sup>45</sup> Khan *et al.* followed a different approach and used short-chain aminosilane inhibitors on  $\text{SiO}_2$ , which have also been used as an Si precursor for  $\text{SiO}_2$  ALD.<sup>46</sup> Furthermore, Soethoudt *et al.* used an aminosilane inhibitor and showed that dimethylamino-trimethylsilane (DMA-TMS) can passivate  $\text{SiO}_2$  surfaces, while keeping  $\text{TiO}_2$ , TiN, and Ru surfaces available for precursor adsorption.<sup>47</sup>

The blocking of precursors adsorption by inhibitor molecules can be based on two mechanisms: (1) the inhibitor molecules can physically cover the surface and thereby prevent the adsorption of precursor molecules due to steric shielding; (2) the inhibitor molecules can react with the surface sites (e.g., hydroxyl groups for oxide surfaces) where the precursor would normally adsorb and thereby chemically passivate the surface.<sup>48</sup> It is expected that both mechanisms contribute to the precursor blocking. Considering the first mechanism, a basic requirement is that the inhibitor molecule should cover the non-growth area as much as possible, i.e., adsorb with a high surface density. At first sight, it might be assumed that all the surface sites are occupied when saturation of the inhibitor adsorption is reached, but that is generally not the case. Previous surface functionalization studies show that in general, small molecules do not achieve a full monolayer coverage at saturation conditions,<sup>49–52</sup> which is due to a number of factors, including steric hindrance, and the mechanism of SMI adsorption during vapor-phase dosing. As a consequence of vapor-phase dosing, inhibitor molecules arrive one-by-one on random surface sites, limiting the surface density of inhibitor molecules.<sup>48</sup> Having unoccupied surface

sites on the non-growth area could potentially lead to precursor adsorption, which leads to loss of selectivity. In order to achieve a high selectivity, it is, therefore, essential to obtain high surface packing of inhibitor molecules on the non-growth area.

The packing of molecules on a surface refers to the arrangement of those molecules, in terms of surface density and covered area. To describe the packing of molecules, random sequential adsorption (RSA) simulations can be applied in which objects are placed on a surface or in a volume in a sequential order.<sup>53–55</sup> RSA simulations have been performed for a wide range of phenomena in different fields from physical chemistry and biology to the car-parking problem.<sup>56</sup> In a RSA model, a  $d$ -dimensional space (e.g., a substrate) is filled by randomly placing objects (e.g., molecules) one-by-one. In this procedure, objects remain frozen on the substrate after they are placed. For each placed object, the model checks for steric overlap with the previously placed objects, and in the case of overlap, the new object is removed.<sup>57,58</sup> Above a limiting coverage, no more objects can be added without having overlap with other objects. This state is called as the “jamming limit,” or the “saturation limit” of the object on the substrate.<sup>59</sup> This jammed state can only contain gaps in between the objects that are too small to fit a new object. For the hard spheres added sequentially to a  $d$ -dimensional volume, the coverage,  $\theta(\tau)$ , approaches to its jamming limit,  $\theta(\infty)$ , as  $\theta(\infty) - \theta(\tau) \sim \tau^{-1/d}$  with  $\tau$  being the time.<sup>60</sup> Consequently, for a two-dimensional RSA model of placing disks on a continuum substrate,  $\theta(\tau)$  asymptotically approaches saturation [i.e.,  $\theta(\infty)$ ] according to  $\theta(\infty) - \theta(\tau) \sim \tau^{-1/2}$ . The jamming limit  $\theta(\infty)$  corresponding to the saturation coverage for disks on a substrate is reported to be 0.55.<sup>55</sup> A subcategory of RSA models, referred to as lattice RSA, considers the placing of objects on a regular pattern of positions.<sup>58,61</sup> The functionalization of a surface with inhibitor molecules can be represented by the two-dimensional lattice RSA model of a structured pattern of surface sites (i.e., crystalline surface). Instead of the aforementioned expression, in lattice RSA, the coverage exponentially approaches the jamming limit as  $\theta(\infty) - \theta(\tau) \sim Ae^{-\tau/\sigma}$ , where  $A$  and  $\sigma$  are parameters that depend on the shape and the orientational freedom of the objects, respectively.<sup>61,62</sup>

RSA simulations can provide valuable insights into the packing and surface density of molecules adsorbed on a surface, and can help in the design of novel area-selective ALD processes. RSA simulations can be considered as a fast method to obtain insights about ASD by considering the steric hindrance during the adsorption process. These simulations are based on the simplest available physical data, i.e., the physical dimensions and shape of the adsorbed inhibitor (or precursor) molecules, and the type and dimensions of the surface lattice. Hence, they do not require high computing power. Since RSA does not consider thermodynamic or kinetic data as previously presented kinetic Monte Carlo methods,<sup>63,64</sup> this method also does not require complex theoretical or experimental preparation. Therefore, RSA simulations allow for fast screening of inhibitor molecules during the design of ASD processes. The use of RSA simulations for area-selective ALD is inspired on previous studies by Khan *et al.*, where the stochastic packing of the bis( $N,N$ -dimethylamino)dimethylsilane (DMADMS) inhibitor on a  $\text{SiO}_2$  surface was investigated.<sup>46</sup> RSA simulations were also used in our earlier work to obtain understanding of how steric hindrance effects limit the coverage of SMIs on a surface.<sup>37</sup>

In this work, we explore the use of RSA simulations to obtain an understanding of the packing of SMIs on a surface and its influence on precursor blocking. We first establish the method of performing RSA simulations by investigating the packing of virtual inhibitor molecules, i.e., molecules with a specific size and shape, not necessarily representing actual molecules. Furthermore, analysis methods were developed for obtaining quantitative information on the precursor blocking from RSA simulations. Combined with density functional theory (DFT) simulations, the developed RSA simulations and statistical analysis were applied to interpret the differences in precursor blocking of ethanol as compared to Hacac. Based on this methodology, the paper is organized as follows: The methods for the experimental studies and DFT simulations are described in Sec. II, whereas the development and optimization of the RSA simulations are discussed in Sec. III. RSA simulations of virtual inhibitor molecules are discussed in Sec. IV. In Sec. V, the RSA simulations are validated by comparing to experimental results using alcohol inhibitor molecules during area-selective ALD. Finally, the work is summarized in Sec. VI.

## II. METHODS

### A. ALD processes and *in situ* spectroscopic ellipsometry (SE)

The ALD processes were performed in an Oxford Instruments FlexAL reactor. A detailed description of the reactor can be found in Ref. 65. In brief, it consists of a vacuum chamber, a pumping system, a remote inductively coupled plasma (ICP) source, a 200 mm substrate table, and a loadlock. The process for deposition of SiO<sub>2</sub> by plasma-assisted ALD is based on the recipe developed by Dingemans *et al.* with bis(diethylamino)silane (BDEAS) and O<sub>2</sub> plasma pulses.<sup>66</sup> During every ABC-type ALD cycle, an inhibitor dosing step was performed as step A with a typical dosing time of 10 s. Acetylacetone (Hacac) (Wacker Chemie AG, ≥99.5%, CAS: 123-54-6), methanol (Merck KGaA, ≥99.9%, CAS: 67-56-1), ethanol (Merck KGaA, ≥99.9%, CAS: 64-17-5), isopropanol (VWR International S.A.S., ≥98%, CAS: 67-63-0), 1-propanol (ThermoFisher GmbH, 99.9% anhydrous, CAS: 71-23-8), and 1-butanol (Honeywell, 99.9%, CAS: 71-36-3) were used as inhibitors. All inhibitors were used as received. The inhibitors were kept in stainless steel containers at room temperature and were supplied into the chamber via vapor-drawn dosing. Before the start of the deposition process, the substrates were heated on the substrate table to a temperature of 150 °C for 10 min, while a mixture of Ar and O<sub>2</sub> gas flowed through the chamber at a chamber pressure of 250 mTorr. Subsequently, the substrate was cleaned by a 5 min O<sub>2</sub> plasma treatment. *In situ* spectroscopic ellipsometry (SE) measurements were performed to characterize the film thickness during the deposition using a J.A. Woollam M2000D ellipsometer with a photon energy range of 1.3–5.0 eV at an incidence angle of 70°. The film thickness of SiO<sub>2</sub> was fitted by modeling the acquired data with a Cauchy parameterization.<sup>38</sup>

### B. DFT calculations

The electronic energies were calculated using the Vienna *Ab initio* simulation package (VASP),<sup>67–70</sup> as implemented in MedeA-VASP software package.<sup>71</sup> The adsorption configurations of

the alcohol molecules were determined using the generalized gradient approximation (GGA) functional by Perdew, Burke, and Ernzerhof (PBE),<sup>72</sup> the dispersion correction D3 and the Becke–Johnson (BJ) damping function,<sup>73,74</sup> and the projected augmented wave formalism (PAW) with a plane wave cutoff of 400 eV.<sup>75</sup> The self-consistent field cycle was converged with an accuracy of 10<sup>−5</sup> eV and the geometry was optimized until the forces were less than 10<sup>−2</sup> eV Å<sup>−1</sup>. The Brillouin zone was sampled by a gamma-centered 2 × 2 × 1 Monkhorst–Pack<sup>76</sup> grid and a Gaussian smearing of 0.1 eV was used. The Al<sub>2</sub>O<sub>3</sub> surface was modeled following the same procedure as our previous work.<sup>37,48</sup> A 4-layer 3 × 3 supercell of α-Al<sub>2</sub>O<sub>3</sub>(0001) with a vacuum of 17 Å to accommodate the inhibitor molecules, as used in previous studies. The resultant supercell has the a, b, c lattice dimensions of 14.3, 14.3, and 27 Å, respectively, with θ = 120°. The Al<sub>2</sub>O<sub>3</sub> surface is partially hydroxylated by locating hydroxyl groups on all nine top layer Al atoms resulting in a 1 ML–OH coverage (corresponding to 5.1–OH/nm<sup>2</sup>). Nine out of the 18 exposed oxygen atoms below the top layer Al atoms are hydrogenated. The bottom three layers of atoms were kept fixed and the remaining atoms of the slab and the atoms of the adsorbed species were relaxed. The adsorption energies for the alcohol molecules were calculated following Eq. (1), while the adsorption energies for Hacac were determined in a previous study,<sup>37,38</sup>

$$E_{\text{ads}} = E_{(\text{alcohol}/\alpha\text{-Al}_2\text{O}_3)} - [E_{(\text{alcohol})} + E_{(\alpha\text{-Al}_2\text{O}_3)}], \quad (1)$$

where  $E_{(\text{alcohol}/\alpha\text{-Al}_2\text{O}_3)}$  is the energy of the alcohol molecule adsorbed on the α-Al<sub>2</sub>O<sub>3</sub> surface;  $E_{(\text{alcohol})}$  is the energy of an alcohol molecule in the gas phase (modeled using a 30 Å cell size and a 1 × 1 × 1 KPOINT mesh); and  $E_{(\alpha\text{-Al}_2\text{O}_3)}$  is the energy of the (0001) surface of α-Al<sub>2</sub>O<sub>3</sub> without adsorbates.

## III. SETTING UP OF THE RANDOM SEQUENTIAL ADSORPTION SIMULATIONS

For the definition of the RSA simulation, the main assumptions are (1) there are no intermolecular interactions between the adsorbed inhibitors except for 2D steric hindrance; (2) the inhibitor molecules do not desorb from the surface. Regarding the first assumption, it should be noted that steric hindrance between the inhibitor molecules constitutes the main factor determining the packing of molecules on the surface. In contrast to cases when using long-chain molecules to form a SAM, it is assumed that attractive interactions due to, for example, van der Waals forces between the SMIs are too small to play a significant role in the packing.<sup>77</sup> In other words, if we approximate the intermolecular interactions as a simple Lennard–Jones potential,<sup>78</sup> we consider the repulsive term describing Pauli repulsion to account for the steric interactions, but not the attractive long-range term. The second assumption regarding a lack of desorption can be made considering that in practice only molecules that strongly bond to the non-growth area are selected as candidate inhibitor molecules. The validity of these two assumptions is assessed for specific examples in Sec. V.

The RSA simulations were developed based on previous works on lattice RSA simulations.<sup>37,61,79</sup> The RSA simulation procedure is described in Fig. 1. A simplified model of the inhibitor molecule was generated by considering its “footprint,” i.e., the projection of

the 3D shape of the molecule onto the 2D surface. A random site is chosen and the simulated molecule is temporarily placed on this position. If no overlap is detected between this molecule and any other molecule on the surface, it is permanently placed on that position. Otherwise, the molecule starts to rotate with a specific rotation step size until no overlap is detected. If the molecule does not fit after a full rotation of  $2\pi$  rad, the molecule is removed from that position, and the procedure starts again at another random site. This

procedure is repeated until all the surface sites are checked and the saturated coverage is reached, i.e., no more molecules can adsorb on the surface. Following this procedure, three different cases were studied in the following sections of this work. In [Sec. IV](#), the packing of the “virtual” inhibitor molecules with a circular shape and various sizes has been investigated. [Section V](#) considers two inhibitors (i.e., ethanol and Hacac) that were also studied experimentally. Before starting those simulations, optimal settings to have accurate

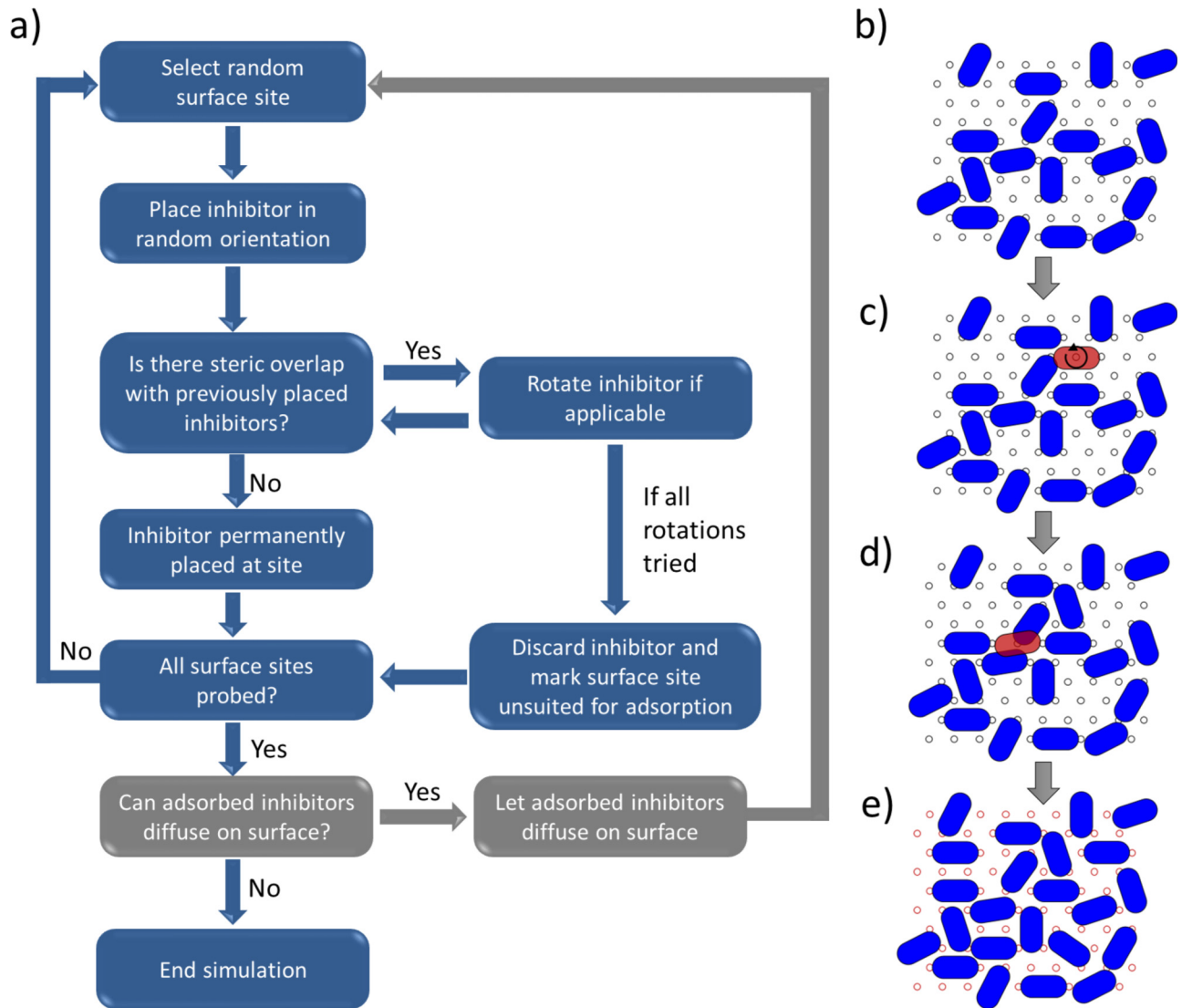


**FIG. 1.** Random sequential adsorption (RSA) simulation procedure for studying inhibitor adsorption. (a) Simulation flow scheme for the simulations performed in this work. The last two steps related to surface diffusion (depicted in gray) are only considered for the simulations presented in [Secs. III C](#) and [V C](#). (b)–(e) Illustrations of the surface during different stages of the RSA simulation from low coverage (b) to saturation (e). (b) For each iteration, a random surface site is selected onto which an inhibitor molecule is placed in a random orientation. In case there is no steric overlap with previously placed inhibitors, the molecule is permanently adsorbed on the surface at that location. (c) If there is overlap, different orientations are tried. (d) In case none of the orientations fit, the molecule is removed from the simulation and the surface site is marked as unsuited for inhibitor adsorption. (e) The simulation continues until all sites have been tried resulting in a saturated surface.

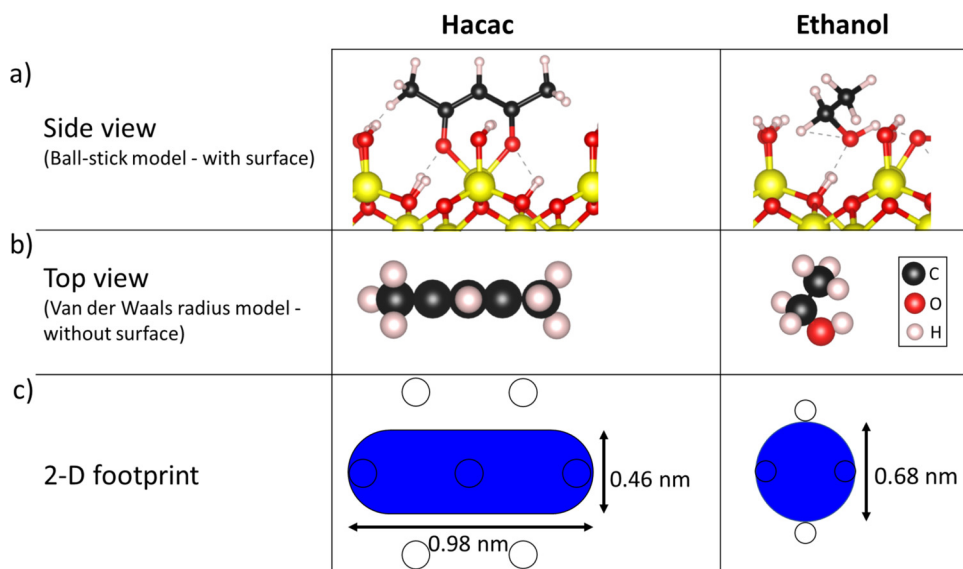


**FIG. 2.** (a) Side and (b) top views of DFT optimized Hacac and ethanol molecules adsorbed on an  $\text{Al}_2\text{O}_3$  (0001) surface and (c) details of the footprints used in the RSA simulations. The circles on the bottom row images represent the surface adsorption sites, whereas the blue footprints show the DFT-calculated position of the inhibitors on the non-growth area.

simulation results [such as boundary conditions, simulation cell size (Sec. III A), and rotational degree of freedom of the molecules on the model surface (Sec. III B)] were studied.

### A. Influence of system size and boundary conditions on the accuracy of RSA simulations

For all simulations presented in this work, a hexagonal lattice with a lattice constant of 0.48 nm is created to represent the (0001) surface of  $\alpha\text{-Al}_2\text{O}_3$ , which is the most stable phase of  $\text{Al}_2\text{O}_3$ .<sup>80,81</sup> Here,  $\text{Al}_2\text{O}_3$  is chosen as the non-growth area, while the surface can be changed to understand the functionalization of other materials. By using the 2D footprint of the Hacac molecule as shown in Fig. 2, surface densities of Hacac molecules at saturation coverage were calculated on a substrate with a hard boundary, without a boundary, and with periodic boundary conditions as shown in Fig. 3. These calculations were repeated for substrates with different surface areas and the corresponding surface Hacac densities are reported in Fig. 3(d). These results show that no-boundary conditions always results in the highest Hacac surface density, whereas the substrate with hard boundary conditions has the lowest surface density due to the difference in utilization of the edge adsorption sites. In an infinitely large simulation cell, all boundary conditions converge to the same value. Although the periodic boundary conditions, in principle, give the most accurate results, in this study, the target substrate was modeled using no-boundary conditions. However, a substrate with a relatively large surface area of  $2680 \text{ nm}^2$  is used for the simulations reported in Secs. III and IV, for which the Hacac saturation lies within  $\pm 2\%$  of the saturation results from periodic boundary conditions.

### B. Influence of rotational freedom on packing

Based on DFT results of the adsorption of the alcohol molecules on the  $\text{Al}_2\text{O}_3$  (0001) surface (as reported in Sec. V), ethanol molecules are modeled as disks to be adsorbed on the

bridge sites of the hexagonal lattice, whereas Hacac molecules (DFT modeled in a previous study),<sup>38</sup> are modeled as discor-ectangles (also known as a stadium or obround shape) whose center is positioned on the Al top site. These two models are shown in Fig. 2. Due to their circular symmetry, the rotational freedom of ethanol molecules does not need to be taken into account. For Hacac however, the rotational state of the molecule is important due to the discor-ectangular footprint area of the molecule, see the inset of Fig. 4. The DFT calculations in Ref. 37 report the most stable DFT-optimized Hacac geometry. In the chelate configuration (see Fig. 2), the oxygen atoms of the Hacac molecule interact with the sublayer vicinal OH groups through hydrogen bonds. When considering this configuration for the RSA simulations, only one rotational state (or two states in twofold symmetry, see the inset of Fig. 4), is possible on the surface. If there are more H atoms bonded to the neighboring O sites, then the Hacac molecule has six relevant rotational states ( $60^\circ$  rotational step size). However, in experimental conditions, Hacac likely does not only adsorb in the most favorable adsorption geometry, which may result in many different rotational configurations. Therefore, in order to determine a reasonable rotation step for the simulations (which is also used as the coefficient of the starting placement angle), different rotation step sizes were tested as shown in Fig. 4. According to obtained data, when the rotation of Hacac molecules is constrained to the DFT-calculated positions as explained above (i.e.,  $60^\circ$  and  $360^\circ$ ), surface inhibitor densities of 1.1 and 1.2 molecules/ $\text{nm}^2$  were achieved. On the other hand, when the rotation of the Hacac molecules was probed with rotation steps of  $1^\circ$ , a much higher surface density of 1.5 molecules/ $\text{nm}^2$  was calculated. For the range of the rotation steps between  $1^\circ$  and  $9^\circ$ , the results in Fig. 4 were found to be similar within a 1% margin. Therefore, a rotational increment of  $9^\circ$  was chosen for the rest of the RSA simulations to describe unconstrained rotation.

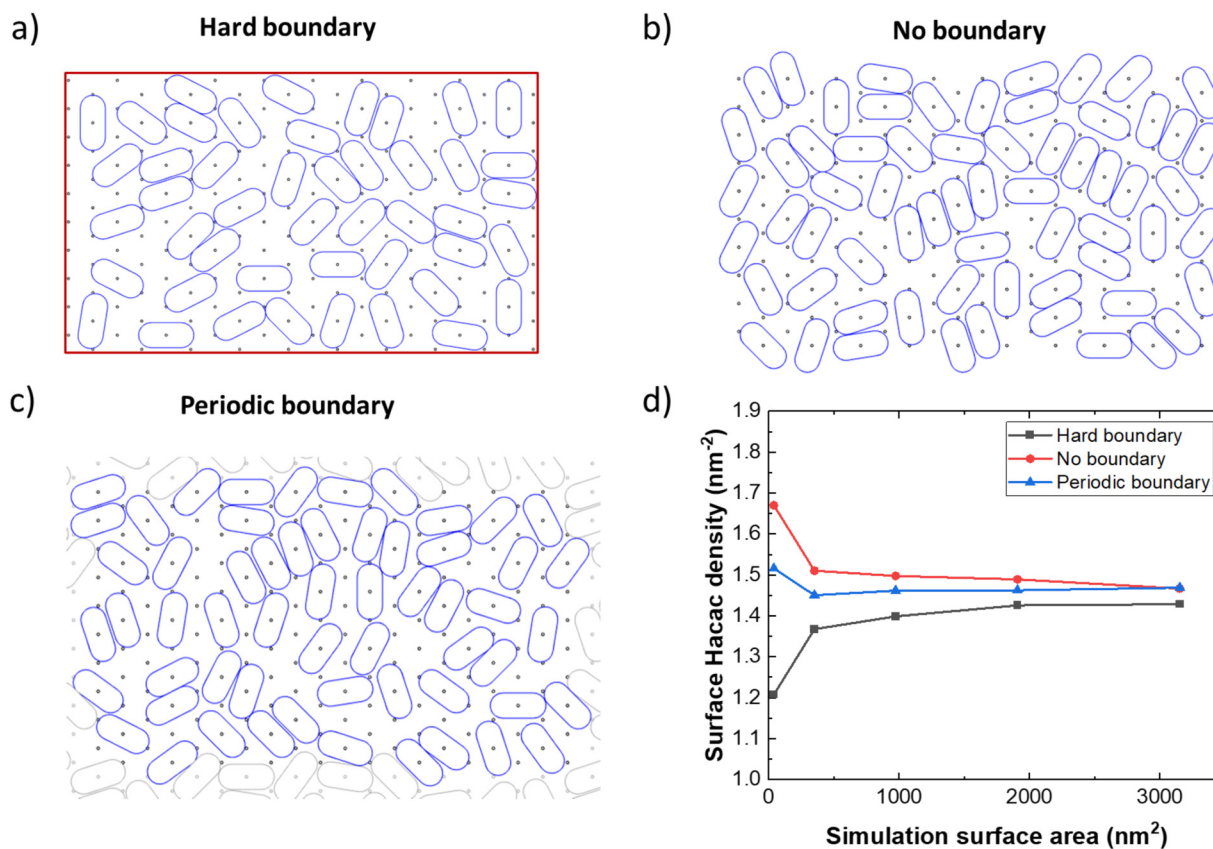


**FIG. 3.** Application of different boundary conditions during RSA simulations. (a) When using hard boundary conditions, molecules are not allowed to exceed system boundaries (red rectangle). (b) For no-boundary conditions, part of the molecules can exceed system boundaries allowing them to adsorb on surface sites on the edge. (c) Periodic boundary conditions work similar to no boundary settings, but parts of the molecules leaving system boundary enters the system from the other side (gray drawing on the figure). A substrate with 38.9 nm<sup>2</sup> surface area is used for the demonstration above. (d) Surface Hacac density (nm<sup>-2</sup>) for different simulation surface sizes and boundary conditions.

### C. Influence of inhibitor diffusion on packing

When adsorbed on the surface, molecules can potentially diffuse driven by the thermal energy. Diffusion of the inhibitor molecules can influence their packing on the surface (e.g., by creating new available sites for adsorption) and may eventually lead to an improved precursor blocking. To allow for more accurate simulations, the RSA simulation procedure was extended, by including the steps depicted in gray in Fig. 1, in order to understand the impact of surface diffusion on the arrangement of inhibitor molecules.<sup>82</sup> This extended procedure is as follows: (1) the packing of the inhibitor molecules is first simulated without considering surface diffusion; (2) all the inhibitor molecules adsorbed on the surface are allowed to diffuse with a certain probability, which is related to the diffusion energy barrier; (3) all the surface sites are checked again to determine if more inhibitor molecules can be added on the surface. These last two steps are referred to as one simulation iteration, and these iterations were repeated to determine the final packing of the inhibitor molecules.

It is crucial to know the diffusion energy barrier to investigate the surface diffusion of inhibitor molecules. The probability for surface diffusion ( $P$ ) is determined by Eq. (2),

$$P = \nu_0 \exp\left(-\frac{E_{diff}}{k_B T}\right) \tau, \quad (2)$$

where  $\nu_0$  (in s<sup>-1</sup>) is the attempt frequency of the surface diffusion corresponding to the lattice vibration,  $k_B$  is the Boltzmann constant (in eV/K),  $E_{diff}$  is the diffusion barrier (in eV),  $T$  is the substrate temperature (in K), and  $\tau$  is the time period for one simulation iteration (in s).<sup>83</sup> The value of  $\nu_0$  is estimated to be 10<sup>10</sup> s<sup>-1</sup> for organic molecules based on experimental studies,<sup>84</sup> and the temperature during ALD is typically in the range of 100–300 °C. For the case that no chemical bond is formed between the surface and the adsorbed molecule, the diffusion energy barrier  $E_{diff}$  can be estimated from the desorption energy  $E_d$  via the formula  $E_{diff} = \alpha E_d$ , where  $\alpha$  is the corrugation ratio.<sup>82,83,85,86</sup> The value of  $\alpha$  may range from 0.1 to 0.8 depending on the molecule and surface and on



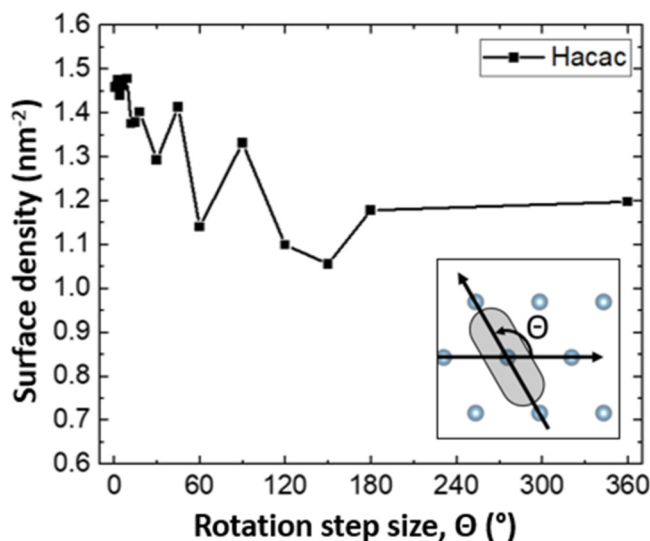


FIG. 4. Change of Hacac density with respect to rotation step size. Due to size and the geometry of Hacac molecules, the rotation step size influences the packing of the molecules on a hexagonal  $\text{Al}_2\text{O}_3$  lattice.  $180^\circ$  and  $360^\circ$  cases mean no effective rotation during the simulation.

whether a crystalline or amorphous surface is considered,<sup>82,83,85,86</sup> which translates into a fairly broad range for the diffusion energy barrier. To examine the potential influence of inhibitor diffusion on the packing, the extended RSA simulations were performed considering a low (0.1 eV), medium (0.5 eV), and high energy barrier (1.3 eV) as shown in Fig. 5. The simulations reveal that surface diffusion can lead to an increase of the surface coverage of about 30% for low and medium diffusion barriers. The saturation of the covered surface area is illustrated in the inset of Fig. 5, showing the data for the low diffusion barrier on a linear time scale. The exponential approach to the jamming limit, as discussed in the introduction, is clearly visible in this inset image. It should be noted that inhibitors with a low diffusion barrier reach the saturated surface density much faster. The data for a high energy barrier show a constant surface density, implying that no effective diffusion takes place within the 10 s time period of calculation (i.e., typical inhibitor dosing time)  $t$ . Taken together, these simulation results indicate that surface diffusion can help to achieve an increased surface area coverage, which may contribute to an improved precursor blocking.

#### D. Limitations of RSA

Being a very fast and informative approach, RSA simulations rely only on the physical inputs defined during the setup of the simulation. Therefore, chemical properties such as attractive/repulsive interactions between adsorbed molecules or enhancement/depletion of the surface activity as a function of coverage are not considered during the simulations. RSA simulations also do not directly capture the effects of experimental conditions such as temperature and pressure. In addition, the three-dimensional shape of

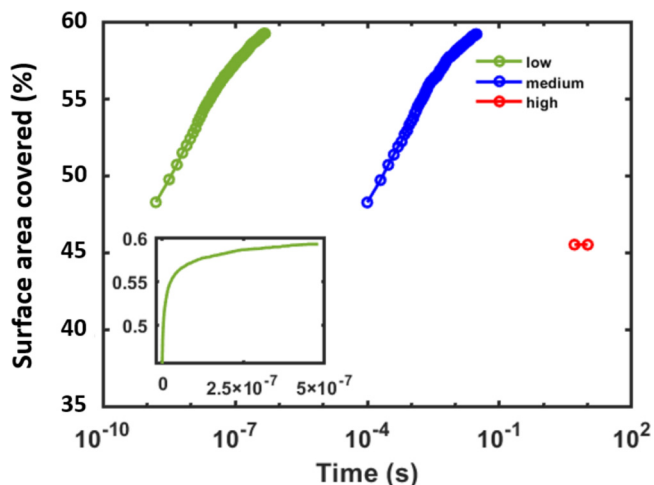


FIG. 5. Calculated surface area covered by inhibitor molecules on an  $\text{Al}_2\text{O}_3$  surface considering low (0.1 eV), medium (0.5 eV), and high (1.3 eV) diffusion energy barriers. The time periods per simulation iteration  $\tau$  are assigned to give probabilities for diffusion of 1, 1, and  $1 \times 10^{-5}$ , respectively [see Eq. (2)]. The starting covered surface area of 0.45 is not shown due to the logarithmic scale on the x axis. The inset depicts the data for the diffusion barrier of 0.1 eV on a linear scale, which clearly shows that the surface coverage is saturated after  $0.5 \mu\text{s}$ .

the molecules and substrate are not considered for the model explained here. When needed, the accuracy of the RSA simulations may be improved by more detailed inputs based on prior experiments or DFT calculations, such as sticking probability as a function of coverage, the contribution of reactive adsorption, more specific packing constraints, or an amorphous surface grid. However, this does not fit the simple and fast nature of the method since experiments and DFT require considerably higher computing power.

#### IV. RSA SIMULATIONS OF THE PACKING OF VIRTUAL INHIBITOR MOLECULES

In this part, the method of using RSA simulations to investigate the packing of inhibitor molecules is employed, considering “virtual” inhibitor molecules with a circular shape and various sizes. Section IV A discusses the general results for circular inhibitor molecules as an example. Subsequently, statistical methods for quantifying the effectiveness of precursor blocking by the inhibitor molecules are introduced in Sec. IV B.

##### A. Simulation definition and general results

First, we will consider the general case of using circular-shaped virtual inhibitor molecules. These molecules were placed on the Al-OH top sites on the  $\text{Al}_2\text{O}_3$  surface in a random sequence until no more inhibitors can adsorb based on the defined constraints from our model. The surface density of the inhibitor molecules ( $N/A$ , with  $N$  being the number of inhibitor molecules and  $A$  the area of the surface) and the fraction of the surface area covered by inhibitor molecules ( $\pi R^2 \cdot N/A$ ) are shown in Fig. 6(a) as a

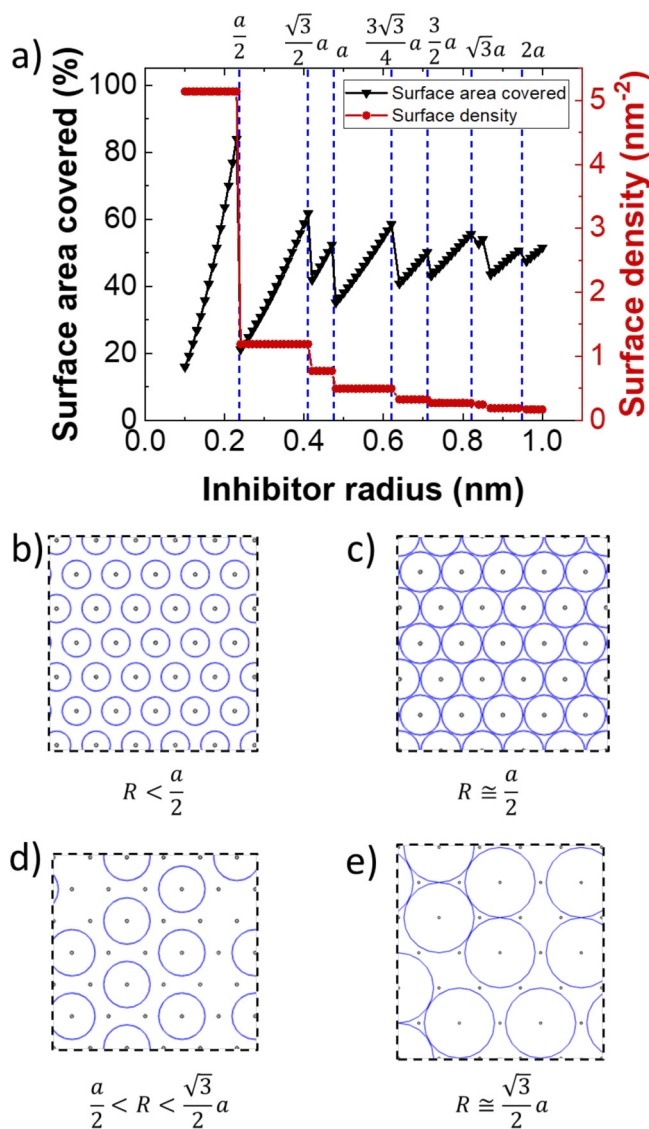


**FIG. 6.** (a) The fraction of surface area covered and the surface density vary as a function of the radius of the inhibitor molecules. (b)–(e) RSA simulation results illustrating the packing of circular-shaped virtual inhibitor molecules with small radii ( $R$ ) as compared to lattice constant ( $a$ ).

function of the radius of the molecule  $R$ . The surface density initially shows a plateau corresponding to the density of the surface sites (i.e.,  $5.2 \text{ nm}^{-2}$ ), but then decreases with the radius of the molecule. The trend of the surface area covered shows that, for circular inhibitors, the maximum covered area is reached when  $R$  equals half of the lattice constant  $a$ , corresponding to the largest inhibitor molecule that can adsorb on all the surface sites without overlap. In our example, the lattice constant for the (0001) surface of  $\alpha\text{-Al}_2\text{O}_3$  is  $0.48 \text{ nm}$ , giving a radius for the maximum surface coverage of  $0.24 \text{ nm}$ . Fig. 6(a) also shows that when  $R$  equals

$\frac{\sqrt{3}}{2}a$ ,  $a$ ,  $\frac{3\sqrt{3}}{4}a$ ,  $\frac{3}{2}a$ ,  $\sqrt{3}a$ , and  $2a$  times of the lattice constant  $a$ , a local maximum of the surface coverage is reached. These local maximums are lower than the global maximum because steric hindrance makes some surface sites unavailable for adsorption of more inhibitor molecules. The analysis illustrated in Fig. 6 indicates that the optimum size of the inhibitor molecule for reaching the maximum surface coverage can be identified based on the results of the RSA simulations.

## B. Quantitative analysis of precursor blocking

To quantify how the packing of inhibitor molecules translates into the blocking of precursor molecules, two different methods were developed based on the RSA simulations. Following the RSA literature, we refer to the positions where no inhibitor molecules are located as “gaps.” Instead of just measuring the gap size, it has to be taken into account that the precursor molecules can only adsorb at specific sites. Note that the inhibitor and precursor molecules might adsorb at different sites within a unit cell (e.g., at the top or bridge site). The capability of gaps to adsorb precursor molecules is analyzed by calculating the smallest distance ( $L_s$ ) from an unoccupied surface site to neighboring inhibitor molecules. The general procedure for calculating this distance is illustrated in Fig. 7(a). Although some surface sites are not occupied after the saturated adsorption of the inhibitors, not all of these unoccupied surface sites are available for the adsorption of precursor molecules due to the steric hindrance between the inhibitor and the precursor. In other words, if a surface site is too close to a neighboring inhibitor molecule, or when a relatively large precursor molecule is employed, there is not enough space for the precursor molecule to adsorb on a specific site. The smallest distance value can be interpreted as the maximum size a (circular-shaped) molecule can have to adsorb in the gap without experiencing steric hindrance caused by the neighboring molecules. We will refer to this value as the “effective gap size.” In analogy to the “radial distribution function” in the continuum RSA literature, statistical analysis of the effective gap size can be performed, which in this case gives insight into the precursor blocking.

Again, we will illustrate this analysis method by considering circular-shaped inhibitors. For all the surface sites that are not covered by an inhibitor molecule, the distances from that surface site to the neighboring inhibitors were calculated [see Fig. 7(a)]. The smallest value of all the calculated distances gives the effective gap size and is included in a histogram as shown in Fig. 7(b). In this case, it is found that there are three distinct types of unoccupied surface sites, marked with numbers in the inset of Fig. 7(b). The histogram thereby illustrates that the statistical analysis of the effective gap size can also help to identify different types of unoccupied surface sites. Figure 7(b) shows that there are fewer large gaps, which suggests that large precursor molecules are easier to block. More importantly, the statistical analysis provides a quantitative method to describe the precursor blocking by a specific inhibitor molecule. For example, if a precursor molecule has a van der Waals radius of  $0.3 \text{ nm}$  (i.e., roughly the van der Waals radius of adsorbed BDEAS precursor with both amino ligands eliminated,  $-\text{SiH}_2$ ) as indicated by the dashed line in Fig. 7(b), all the surface sites on the left of the dashed line do not provide enough space for the

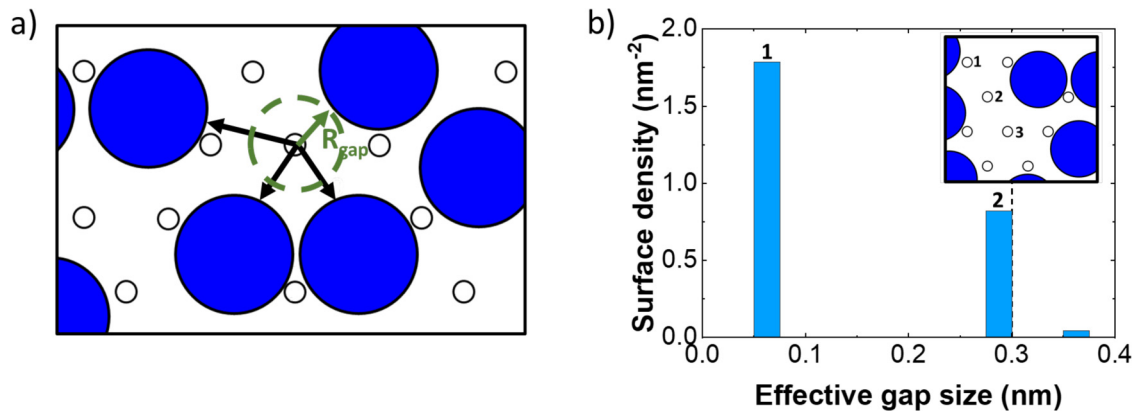


**FIG. 7.** (a) Schematic illustration of the procedure of determining the effective size of the gap in between inhibitor molecules after saturated adsorption, taking the site where the precursor adsorbs into account. (b) Histogram showing the statistical analysis of the effective gap size for this example. The surface density of gaps depends strongly on their sizes. The dashed line at 0.3 nm marks the size of a BDEAS precursor.

precursor molecule to adsorb. This means that only the sites marked with number 3 are available for precursor adsorption. The sum of the number densities at the right of the dashed line gives a measure for the number of precursor molecules that can potentially adsorb on the surface; in this case, giving a low surface density of  $0.03 \text{ nm}^{-2}$ .

The method described above gives the number of gaps available for the adsorption of precursor molecules with a certain size, but it does not directly provide information on the packing and distribution of the precursor molecules on the surface. Therefore, a second analysis method was developed to calculate the adsorption of precursor molecules on a surface functionalized with inhibitor molecules. In the simulation corresponding to Fig. 8(a), circular-shaped precursor molecules were adsorbed on the unoccupied

surface sites of a surface functionalized with inhibitor molecules. The surface densities for precursor molecules with different radii are plotted in Fig. 8(b), showing that the surface density of adsorbed precursor molecules decreases as the size of the precursor increases. In agreement with the results shown in Fig. 6(a), the graph shows a constant surface density for radii between 0.06 and 0.24 nm due to the occupancy of all type 2 and 3 surface sites. The surface density drops to zero at a radius of 0.40 nm, which illustrates that precursor molecules with a radius above 0.40 nm should be blocked effectively with this virtual inhibitor molecule. Although the current analysis is performed by assuming inhibitor and precursor molecules with circular footprints, the size and the shape of the inhibitor and precursor molecules can be adjusted to predict the behavior of other systems.

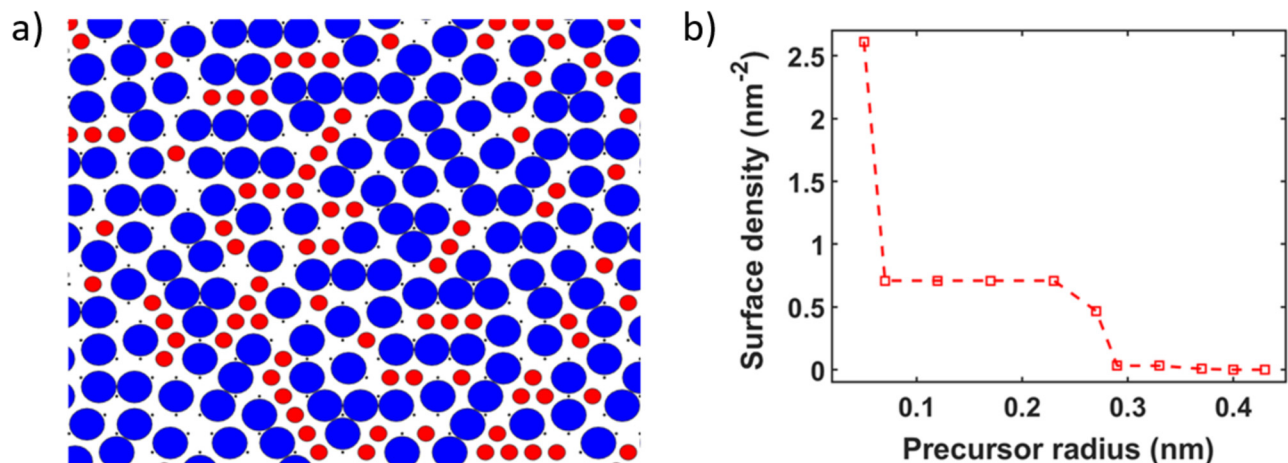


**FIG. 8.** (a) RSA simulation result on the adsorption of precursor molecules (red circles) with a relatively small size (0.17 nm) as compared to the inhibitor molecules (blue circles, 0.35 nm) on an  $\text{Al}_2\text{O}_3$  surface. (b) The surface density of the precursor molecules varies significantly as the radius of the precursor molecule changes.

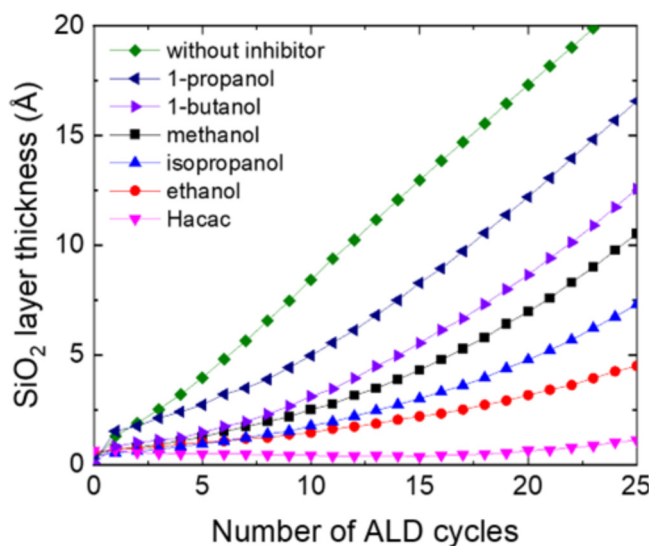


FIG. 9. Nucleation curves for ABC-type  $\text{SiO}_2$  ALD on  $\text{Al}_2\text{O}_3$  non-growth area using various alcohol molecules as an inhibitor. The data of Hacac are presented as Ref. 38.

## V. RESULTS FOR ALCOHOL INHIBITOR MOLECULES

### A. Nucleation for ABC-type ALD cycles

In this section, we present an experimental study on area-selective ALD of  $\text{SiO}_2$  using various alcohol molecules as inhibitors. *In situ* spectroscopic ellipsometry was performed to measure nucleation curves during ALD of  $\text{SiO}_2$  on an  $\text{Al}_2\text{O}_3$  non-growth area. As shown in Fig. 9,  $\text{SiO}_2$  grows on  $\text{Al}_2\text{O}_3$  without a nucleation delay when no inhibitor dose was included in the ALD cycle, and the growth per cycle (GPC) is determined to be 0.09 nm/cycle. Nucleation delays were observed for all ABC-type ALD cycles using alcohol inhibitors, indicating that these inhibitors can adsorb on the  $\text{Al}_2\text{O}_3$  surface and block the adsorption of the BDEAS precursor. Eventually, all the nucleation curves evolve toward linear growth with a GPC of 0.09 nm/cycle, suggesting that the alcohols do not adsorb on  $\text{SiO}_2$  itself. As a reference, results for area-selective deposition of  $\text{SiO}_2$  using acetylacetone (Hacac) are also included in the graph.<sup>17</sup> It can be observed that none of the alcohol molecules are as effective as Hacac in the blocking of BDEAS adsorption. The nucleation delay varies significantly depending on which inhibitor is employed, revealing differences in precursor blocking by the alcohol molecules. Theoretical analyses presented in the following sections focus on a comparison between ethanol and Hacac since these inhibitor molecules exhibit the best precursor blocking performance among the inhibitors screened in this work.

### B. DFT simulations

In this section, DFT calculations using a partially hydroxylated  $\alpha\text{-Al}_2\text{O}_3$  (0001) surface are presented to give insight into the adsorption configuration and bonding of alcohol molecules, which

are used as an input for the RSA simulations described in Sec. IV C. This surface model was chosen for consistency with previous studies on the Hacac inhibitor<sup>37,38</sup> and is used to compare the effectiveness of alcohol inhibitors. For all alcohol molecules investigated, molecular adsorption in between OH surface groups (see Fig. 10) was found to be the most favorable due to the increased hydrogen bond interactions, leading to additional stabilizations of the adsorbate. We ruled out the contribution of cooperative effects on the molecular adsorption of alcohols, see results in Fig. S1 in the supplementary material.<sup>93</sup> In addition, the dissociative chemisorption pathways involving the dissociation of the C–OH bond of the alcohol molecule and the O–H bond of a surface hydroxyl group to form  $\text{H}_2\text{O}_{(g)}$  as a by-product were also investigated in Table S1 in the supplementary material.<sup>93</sup> As seen in Table S1 in the supplementary material,<sup>93</sup> the adsorption energy becomes less favorable from molecular to dissociative chemisorption, thus, it is not expected for the alcohol molecules to adsorb through dissociative chemisorption. Therefore, only the adsorption of alcohols through molecular adsorption is considered in the RSA simulations presented in the next section. The adsorption energies of the studied alcohol molecules are also supplied in Fig. 10.

### C. Analysis of precursor blocking based on RSA simulations

Experimental data presented in Sec. IV A reveals that Hacac is able to block BDEAS adsorption more effectively as compared to ethanol. In this section, the packing of Hacac and ethanol and their precursor blocking performance are analyzed with RSA simulations using the results of the DFT simulations as input. Our reference case, the Hacac molecule, is discussed first. Previous DFT calculations indicated that Hacac molecules adsorbed in the chelate configuration (i.e., with both of its oxygen atoms bonded to the same  $\text{Al}^{3+}$  surface site) are able to effectively block BDEAS precursor adsorption, while Hacac adsorbed in the monodentate configuration can be displaced by the BDEAS precursor.<sup>37</sup> Therefore, the packing of Hacac molecules on an  $\text{Al}_2\text{O}_3$  surface was simulated by considering the chelate configuration, for which the results are shown in Fig. 11 (a). Based on the size and shape of the Hacac molecule, a discorectangle is used to represent the footprint of the adsorbed Hacac molecule on an  $\text{Al}_2\text{O}_3$  surface. According to our analysis, adsorbed Hacac molecules cover 51% of the surface area used in the model corresponding to a surface inhibitor density of 1.46 Hacac molecules/ $\text{nm}^2$ . Surface diffusion and inhibitor displacement do not play a role for Hacac in the chelate configuration due to the strong chemisorption with a binding energy of  $-1.24$  eV on the surface.<sup>37</sup>

An additional consideration to take into account for the analysis of area-selective ALD of  $\text{SiO}_2$  is that the BDEAS precursor can adsorb on the surface through two different reaction pathways, that is, via elimination of either one or two precursor ligands,<sup>87–89</sup> leading to the adsorption in the form of  $\text{O-SiH}_2(\text{NEt})$  or  $\text{O}_2\text{-SiH}_2$  species, respectively. Correspondingly, two different sites can be identified where a BDEAS precursor molecule can adsorb: the black points (i.e., top sites) in Fig. 11(a) represent the adsorption positions of  $\text{O-SiH}_2(\text{NEt})$  species and the orange points (i.e., bridge sites) represent the adsorption positions of  $\text{O}_2\text{-SiH}_2$  species. It should be noted that BDEAS precursors prefer to adsorb by

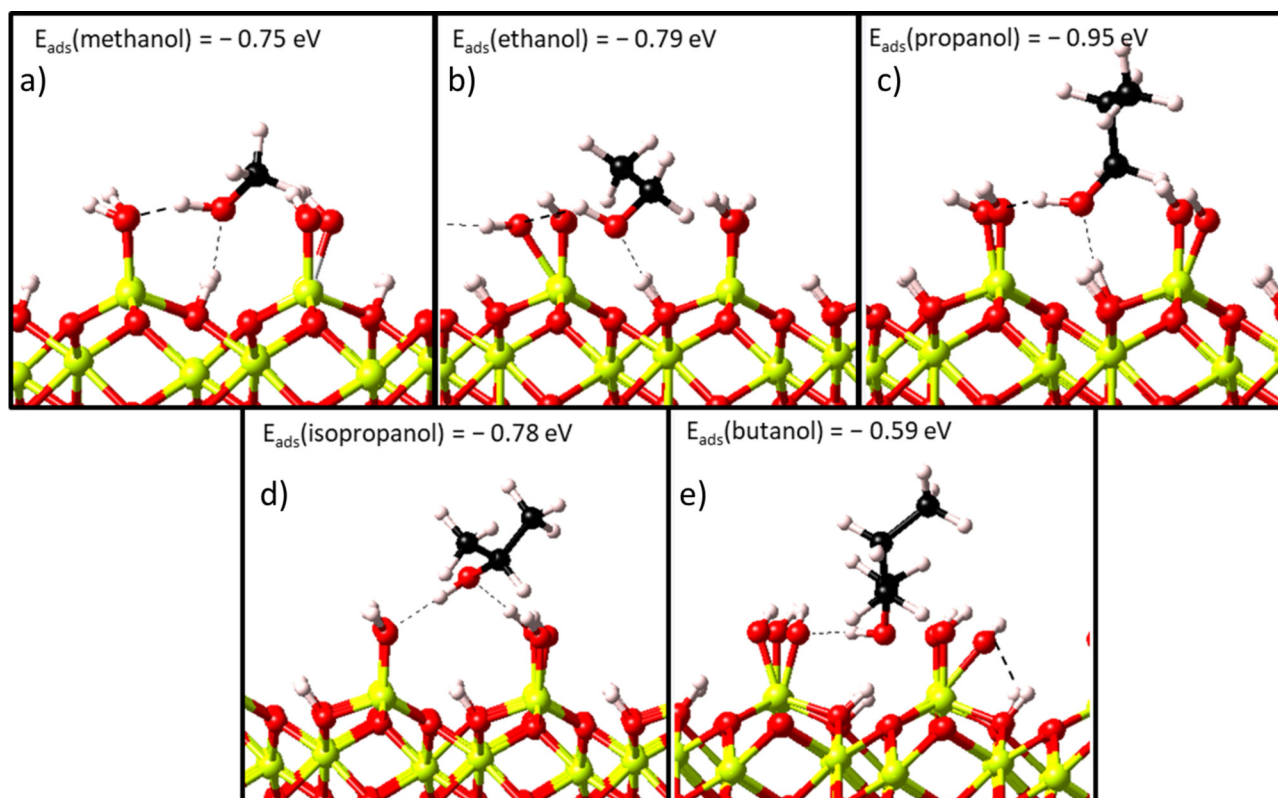


**FIG. 10.** DFT results for the most favorable molecular adsorption configuration of (a) methanol, (b) ethanol, (c) 1-propanol, (d) isopropanol, and (e) butanol on an  $\text{Al}_2\text{O}_3$  surface. The hydrogen bonds formed between the  $\text{Al}_2\text{O}_3$  surface hydroxyl groups and the alcohol molecules are indicated by the dashed lines. [Al: yellow (light gray online), O: red (gray online), C: black, H: white.]

elimination of only one ligand in the form of  $\text{O-SiH}_2(\text{NEt})$  as revealed by both theoretical and experimental studies.<sup>90,91</sup> In principle, the blocking should depend on the size of the incoming gas-phase precursor molecule (i.e., including all the ligands), as well as

on the orientation of the precursor molecule relative to the surface, but for simplicity, we only consider the size of the precursor after the (dissociative) adsorption.<sup>45</sup> With the method described in Sec. IV C, the effective gap sizes relative to the  $\text{O-SiH}_2(\text{NEt})$  adsorption

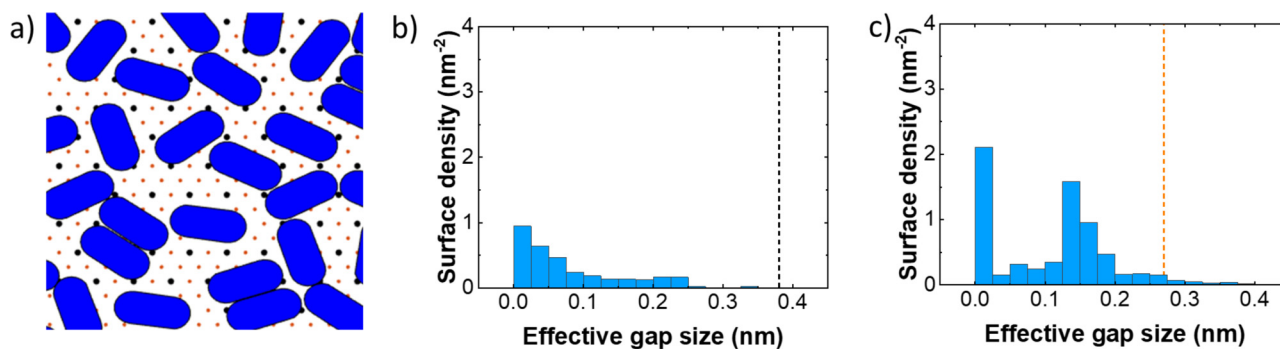


**FIG. 11.** (a) RSA simulation results for the adsorption of Hacac molecules (discoréctangles) on an  $\text{Al}_2\text{O}_3$  surface. The black points represent the surface sites where a BDEAS precursor molecule can potentially adsorb after the elimination of one amino ligand, resulting in  $\text{O-SiH}_2(\text{NEt})$ . The orange (gray online) points represent bridge sites where the BDEAS precursor sits when it bonds to two neighboring hydroxyl sites via the elimination of two amino ligands, resulting in  $\text{O}_2\text{-SiH}_2$ . (b) and (c) Histograms showing the statistics of the effective gap sizes relative to the (b)  $\text{O-SiH}_2(\text{NEt})$  and (c)  $\text{O}_2\text{-SiH}_2$  adsorption positions. The sizes of  $\text{O-SiH}_2(\text{NEt})$  and  $\text{O}_2\text{-SiH}_2$  species are indicated by the dashed lines, respectively.

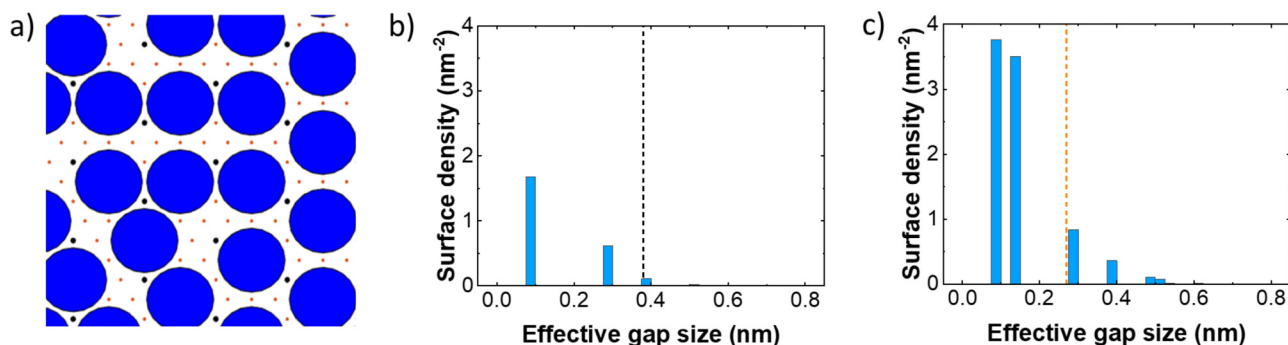


**FIG. 12.** (a) RSA simulation results for the adsorption of ethanol molecules (circles) on  $\text{Al}_2\text{O}_3$  surface considering a diffusion energy barrier of 0.4 eV and displacement ratio of 17%. The black and orange (gray online) points represent the adsorption positions of  $\text{O-SiH}_2(\text{NEt})$  and  $\text{O}_2\text{-SiH}_2$  species, respectively. (b,c) Histograms showing the statistics of the effective gap sizes relative to the (b)  $\text{O-SiH}_2(\text{NEt})$  and (c)  $\text{O}_2\text{-SiH}_2$  adsorption positions. The sizes of  $\text{O-SiH}_2(\text{NEt})$  and  $\text{O}_2\text{-SiH}_2$  species are indicated by the dashed lines, respectively.

positions were determined and presented in Fig. 11(b). The black line at 0.38 nm indicates the van der Waals radius of  $\text{O-SiH}_2(\text{NEt})$  species. It can be observed that all the gaps are on the left of the black line, suggesting that no precursor molecules can adsorb in these gaps. Furthermore, the effective gap sizes relative to the  $\text{O}_2\text{-SiH}_2$  species were also calculated and are shown in Fig. 11(c). In this case, the orange line at 0.27 nm indicates the van der Waals radius of  $\text{O}_2\text{-SiH}_2$  species. Similarly, most of the gaps are not available for adsorption of BDEAS as  $\text{O}_2\text{-SiH}_2$  species. Together, these results provide evidence for the blocking performance by Hacac.

According to the nucleation curves shown in Fig. 9, ethanol is less effective in precursor blocking as compared to Hacac. Based on the DFT results presented in the previous section, the footprint of the ethanol molecule on an  $\text{Al}_2\text{O}_3$  surface is represented by a circle with a radius of 0.34 nm centered at the bridge sites of the surface lattice. In this case, two additional factors need to be considered: (1) surface diffusion, which is mainly determined by the diffusion energy barrier; (2) the displacement of ethanol molecules during the dosing of BDEAS precursor, which was quantified by FTIR measurements. Here, we consider these two factors sequentially, i.e., the calculation results with surface diffusion were used as an input to calculate the influence of displacement on the packing of ethanol. Our DFT calculations show that desorption energy for molecularly adsorbed ethanol on the (0001) surface of  $\text{Al}_2\text{O}_3$  is about  $-0.8$  eV considering a nonactivated pathway. Assuming a corrugation ratio of 0.4, a diffusion energy barrier of 0.3 eV and a time period  $\tau$  0.7  $\mu\text{s}$  [see Eq. (2)] were used in the simulation. The displacement ratio of ethanol during the dosing of BDEAS is determined to be 17% by FTIR measurements (see Fig. S2 in the supplementary material).<sup>93</sup>

The packing of ethanol molecules on an  $\text{Al}_2\text{O}_3$  surface is presented in Fig. 12(a). Based on RSA simulations, ethanol density on the model  $\text{Al}_2\text{O}_3$  surface is determined as 1.29 ethanol molecules/ $\text{nm}^2$ . The adsorbed ethanol molecules cover 61% of the simulated surface area. Similar to the case of Hacac molecule, the distribution of the effective gap sizes was determined and shown in Figs. 12(b) and 12(c). The surface density of the available adsorption sites for  $\text{O-SiH}_2(\text{NEt})$  and  $\text{O}_2\text{-SiH}_2$  is 0.14 and 0.56/ $\text{nm}^2$ , respectively, which is more than the values of 0 and 0.26/ $\text{nm}^2$  with Hacac as the

inhibitor. More surface sites are available when using ethanol as the inhibitor, which is in agreement with shorter nucleation delay observed in the experiments (Fig. 9).

## VI. CONCLUSIONS

In this work, we have developed an analysis method based on RSA simulations to understand the packing of SMIs on a surface in the context of area-selective ALD. A high surface density of inhibitor molecules is the prerequisite for successful blocking precursor adsorption in order to realize area-selective ALD. It was observed that some surface sites are not occupied after saturated adsorption of inhibitor molecules, due to the adsorption at random locations, combined with steric hindrance. At those sites, precursor molecules can potentially adsorb, leading to a loss of selectivity. Based on the results of DFT and RSA simulations, the precursor blocking by Hacac and ethanol inhibitor molecules were analyzed, providing an explanation for the longer nucleation delay that was observed for Hacac. The blocking of precursor adsorption by inhibitor molecules was quantified by performing a statistical analysis of the effective gap sizes in between the adsorbed inhibitor molecules.

The analysis presented in this work provides several new insights into the packing of inhibitors molecules and how the packing corresponds to effective precursor blocking, which can ultimately enable the development of area-selective ALD processes with high selectivity:

- The size and shape of the inhibitor molecule play a critical role in its overall packing on the surface. The optimum size and shape of the inhibitor to achieve a high packing is closely related to the surface distribution of the reactive sites (i.e., lattice constant, symmetry).
- Diffusion of inhibitor molecules increases the surface density, and can thereby improve the precursor blocking. A low diffusion barrier would allow the inhibitors to freely diffuse and form a densely packed layer. It should however be noted that a low diffusion barrier is typically correlated to weak interactions with the surface, potentially also resulting in desorption of the inhibitor.

Consequently, there should be a compromise between surface diffusion and the stability of the inhibitor.

- Some ALD precursor molecules adsorb on the surface through different reaction pathways [e.g., resulting in O–SiH<sub>2</sub>(NEt) and O<sub>2</sub>–SiH<sub>2</sub> species in the case of BDEAS], which increases the requirements for the selection of inhibitor molecules. An inhibitor which can block one reaction pathway may not work as well for other reaction pathway(s), for example, because the pathways may involve different adsorption sites. If several ALD precursor molecules exist for deposition of a certain material, a precursor that reacts through only a single reaction pathway should be preferred, such that the inhibitor can target the blocking of this specific reaction pathway.
- In case it is difficult to achieve a high inhibitor surface density for a given surface, it could also be considered as an alternative strategy to dose two inhibitor molecules with different sizes sequentially. For example, relatively small SMIs can potentially fill the gaps between the main inhibitor molecules to form a densely packed layer of inhibitor molecules on the surface. In the continuum RSA literature, it has been shown that the total surface coverage of binary mixtures of circular disks is higher than the saturated coverage of 0.55 for systems with only one disk.<sup>92</sup>

The presented analysis predominantly focuses on optimizing the inhibitor packing as an essential requirement for effectively blocking ALD precursor adsorption. However, it should be noted that there are several additional requirements for the inhibitor and precursor molecules that need to be considered. For example, depending on the bonding configuration of the inhibitor and the reactivity of the precursor, a fraction of the inhibitor molecules can be displaced from the surface when the precursor is dosed which may contribute to the loss of selectivity.<sup>37,48</sup>

The extensive literature on RSA simulations provides inspiration for studying other effects relevant for area-selective ALD or ALD in general. For example, the mathematical problem of packing circles into a square, also studied using RSA simulations, is of relevance for area-selective ALD using inhibitors on square or line patterns, and can be used to describe the line edge roughness (LER) of structures. Similarly, RSA simulations using a three-dimensional model may be employed to study corner effects for performing area-selective ALD in trenches or on fin structures.

## ACKNOWLEDGMENTS

This publication is based on the work supported by European Research Council (ERC) under the European Union's Horizon 2020 research and innovation programme (Grant Agreement No. 949202) and by Lam Research Corp. M.J.M.M., J.F.W.M., and A.J.M.M. acknowledge support from Vidi project 18363 which is financed by the Dutch Research Council (NWO), and T.E.S. acknowledges support from ANID FONDECYT (Agencia Nacional de Investigación y Desarrollo - Fondo Nacional de Desarrollo Científico y Tecnológico) 11180906. This research was partially supported by the supercomputing infrastructure of the NLHPC (National Laboratory for High Performance Computing Chile) (No. ECM-02). We would like to thank Rik Lengers for contributing to the discussions, and Caspar van Bommel, Jeroen van Gerwen, Cristian van Helvoirt, Joris Meulendijks, Barathi Krishnamoorthy, and Janneke Zeebregts for technical support.

## AUTHOR DECLARATIONS

### Conflict of Interest

The authors have no conflicts to disclose.

### Author Contributions

**J. Li:** Data curation (equal); Methodology (equal); Visualization (equal); Writing – original draft (equal); Writing – review & editing (equal). **I. Tezsevin:** Data curation (equal); Methodology (equal); Visualization (equal); Writing – original draft (equal); Writing – review & editing (equal). **M. J. M. Merkkx:** Data curation (equal); Methodology (equal); Writing – original draft (equal); Writing – review & editing (equal). **J. F. W. Maas:** Writing – review & editing (supporting). **W. M. M. Kessels:** Writing – review & editing (equal). **T. E. Sandoval:** Data curation (equal); Visualization (equal); Writing – original draft (equal); Writing – review & editing (equal). **A. J. M. Mackus:** Conceptualization (lead); Funding acquisition (lead); Project administration (equal); Supervision (lead); Writing – review & editing (lead).

### DATA AVAILABILITY

The data that support the findings of this study are available from the corresponding author upon reasonable request.

## REFERENCES

- 1 I. L. Markov, *Nature* **512**, 147 (2014).
- 2 C. A. Mack, *IEEE Trans. Semicond. Manuf.* **24**, 202 (2011).
- 3 X. Huang *et al.*, *IEEE Trans. Electron Devices* **48**, 880 (2001).
- 4 M. De Marchi, D. Sacchetto, J. Zhang, S. Frache, P.-E. Gaillardon, Y. Leblebici, and G. De Micheli, *IEEE Trans. Nanotechnol.* **13**, 1029 (2014).
- 5 G. S. May and S. M. Sze, *Fundamentals of Semiconductor Fabrication* (Wiley, New York, 2004).
- 6 G. S. May and C. J. Spanos, *Fundamentals of Semiconductor Manufacturing and Process Control* (John Wiley & Sons, Inc., Hoboken, NJ, USA, 2006).
- 7 R. Clark, K. Tapily, K.-H. Yu, T. Hakamata, S. Consiglio, D. O'Meara, C. Wajda, J. Smith, and G. Leusink, *APL Mater.* **6**, 058203 (2018).
- 8 E. Buitrago, M. Meeuwissen, O. Yildirim, R. Custers, R. Hoefnagels, G. Rispens, M. Vockenhuber, I. Mochi, R. Fallica, Z. Tasdemir, and Y. Ekinici, "State-of-the-art EUV materials and processes for the 7nm node and beyond," in *Proc. SPIE Conference Series*, edited by E. M. Panning and K. A. Goldberg (SPIE Advanced Lithography, San Jose, 2017), Vol. 10143, p. 101430T, 8 pp.
- 9 J. Mulkens, M. Hanna, B. Slachter, W. Tel, M. Kubis, M. Maslow, C. Spence, and V. Timoshkov, "Patterning control strategies for minimum edge placement error in logic devices," in *Proc. of SPIE*, edited by M. I. Sanchez and V. A. Ukraintsev (SPIE Advanced Lithography, San Jose, 2017), Vol. 10145, p. 1014505, 13 pp.
- 10 P. Gupta, A. B. Kahng, S. V. Muddu, and S. Nakagawa, "Modeling edge placement error distribution in standard cell library," in *Proc. SPIE*, edited by A. K. K. Wong and V. K. Singh (SPIE 31st International Symposium on Advanced Lithography, San Jose, 2006), Vol. 6156, p. 61560S, 12 pp.
- 11 J. Mulkens, M. Hanna, H. Wei, V. Vaenkatesan, H. Megens, and D. Slotboom, "Overlay and edge placement control strategies for the 7nm node using EUV and ArF lithography," in *Advanced Lithography*, edited by O. R. Wood and E. M. Panning (SPIE Advanced Lithography, San Jose, 2015), p. 94221Q.
- 12 K. Mistry *et al.*, *IEEE Int. Electron Devices Meet.* **247**, 2007 (2007).
- 13 H. Kim, H.-B.-R. Lee, and W.-J. Maeng, *Thin Solid Films* **517**, 2563 (2009).
- 14 R. W. Johnson, A. Hultqvist, and S. F. Bent, *Mater. Today* **17**, 236 (2014).
- 15 V. Cremers, R. L. Puurunen, and J. Dendooven, *Appl. Phys. Rev.* **6**, 021302 (2019).

- <sup>16</sup>S. M. George, *Chem. Rev.* **110**, 111(2010).
- <sup>17</sup>R. L. Puurunen, *J. Appl. Phys.* **98**, 016102 (2005).
- <sup>18</sup>M. Leskelä and M. Ritala, *Angew. Chem., Int. Ed.* **42**, 5548 (2003).
- <sup>19</sup>N. Biyikli, A. Haider, P. Deminsky, and M. Yilmaz, "Self-aligned nanoscale processing solutions via selective atomic layer deposition of oxide, nitride, and metallic films," in *Low-Dimensional Materials and Devices*, edited by N. P. Kobayashi, A. A. Talin, A. V. Davydov, and M. S. Islam (SPIE, San Jose, 2017), 20 pp.
- <sup>20</sup>F. Lazzarino, N. Mohanty, Y. Feurprier, L. Huli, V. Luong, M. Demand, S. Decoster, V. Vega Gonzalez, J. Ryckaert, R. R. H. Kim, A. Mallik, P. Leray, C. Wilson, J. Boemmels, K. Kumar, K. Nafus, A. DeVilliers, J. Smith, C. Fonseca, J. Bannister, S. Scheer, Z. Tokei, D. Piumi, and K. Barla, "Self-aligned block technology: a step toward further scaling," in *Proc. SPIE*, edited by S. U. Engelmann and R. S. Wise (SPIE Advanced Lithography, San Jose, 2017), p. 1014908.
- <sup>21</sup>A. Mameli, Y. Kuang, M. Aghae, C. K. Ande, B. Karasulu, M. Creatore, A. J. M. Mackus, W. M. M. Kessels, and F. Roozeboom, *Chem. Mater.* **29**, 921 (2017).
- <sup>22</sup>A. J. M. MacKus, J. J. L. Mulders, M. C. M. Van De Sanden, and W. M. M. Kessels, *J. Appl. Phys.* **107**, 116102 (2010).
- <sup>23</sup>A. Haider, P. Deminsky, T. M. Khan, H. Eren, and N. Biyikli, *J. Phys. Chem. C* **120**, 26393 (2016).
- <sup>24</sup>B. Kalanyan, P. C. Lemaire, S. E. Atanasov, M. J. Ritz, and G. N. Parsons, *Chem. Mater.* **28**, 117 (2016).
- <sup>25</sup>S. McDonnell *et al.*, *J. Phys. Chem. C* **117**, 20250 (2013).
- <sup>26</sup>E. Färm, M. Vehkamäki, M. Ritala, and M. Leskelä, *Semicond. Sci. Technol.* **27**, 074004 (2012).
- <sup>27</sup>A. J. M. Mackus, M. J. M. Merckx, and W. M. M. Kessels, *Chem. Mater.* **31**, 2 (2019).
- <sup>28</sup>E. K. Seo, J. W. Lee, H. M. Sung-Suh, and M. M. Sung, *Chem. Mater.* **16**, 1878 (2004).
- <sup>29</sup>F. S. Minaye Hashemi, B. R. Birchansky, and S. F. Bent, *ACS Appl. Mater. Interfaces* **8**, 33264 (2016).
- <sup>30</sup>M. D. Sampson, J. D. Emery, M. J. Pellin, and A. B. F. Martinson, *ACS Appl. Mater. Interfaces* **9**, 33429 (2017).
- <sup>31</sup>E. Färm, M. Kemell, M. Ritala, and M. Leskelä, *Thin Solid Films* **517**, 972 (2008).
- <sup>32</sup>H.-B.-R. Lee, M. N. Mullings, X. Jiang, B. M. Clemens, and S. F. Bent, *Chem. Mater.* **24**, 4051 (2012).
- <sup>33</sup>L. Lecordier, S. Herregods, and S. Armini, *J. Vac. Sci. Technol. A* **36**, 031605 (2018).
- <sup>34</sup>J. Hong, D. W. Porter, R. Sreenivasan, P. C. McIntyre, and S. F. Bent, *Langmuir* **23**, 1160 (2007).
- <sup>35</sup>J. Yarbrough, A. B. Shearer, and S. F. Bent, *J. Vac. Sci. Technol., A* **39**, 021002 (2021).
- <sup>36</sup>G. N. Parsons and R. D. Clark, *Chem. Mater.* **32**, 4920 (2020).
- <sup>37</sup>M. J. M. Merckx, T. E. Sandoval, D. M. Hausmann, W. M. M. Kessels, and A. J. M. Mackus, *Chem. Mater.* **32**, 3335 (2020).
- <sup>38</sup>A. Mameli, M. J. M. Merckx, B. Karasulu, F. Roozeboom, W. M. M. Kessels, and A. J. M. Mackus, *ACS Nano* **11**, 9303 (2017).
- <sup>39</sup>A. Yanguas-Gil, J. A. Libera, and J. W. Elam, *Chem. Mater.* **25**, 4849 (2013).
- <sup>40</sup>H. B. Profijt, S. E. Potts, M. C. M. van de Sanden, and W. M. M. Kessels, *J. Vac. Sci. Technol. A* **29**, 050801 (2011).
- <sup>41</sup>D. R. Boris, V. D. Wheeler, N. Nepal, S. B. Qadri, S. G. Walton, C. Chip, and R. Eddy, *J. Vac. Sci. Technol. A* **38**, 040801 (2020).
- <sup>42</sup>M. J. M. Merckx, R. G. J. Jongen, A. Mameli, P. C. Lemaire, K. Sharma, D. M. Hausmann, W. M. M. Kessels, and A. J. M. Mackus, *J. Vac. Sci. Technol. A* **39**, 012402 (2021).
- <sup>43</sup>S. Balasubramanyam, M. J. M. Merckx, M. A. Verheijen, W. M. M. Kessels, A. J. M. Mackus, and A. A. Bol, *ACS Mater. Lett.* **2**, 511 (2020).
- <sup>44</sup>M. J. M. Merckx, S. Vlaanderen, T. Faraz, M. A. Verheijen, W. M. M. Kessels, and A. J. M. MacKus, *Chem. Mater.* **32**, 7788 (2020).
- <sup>45</sup>H. G. Kim *et al.*, *Chem. Mater.* **32**, 8921 (2020).
- <sup>46</sup>R. Khan *et al.*, *Chem. Mater.* **30**, 7603 (2018).
- <sup>47</sup>J. Soethoudt, Y. Tomczak, B. Meynaerts, B. T. Chan, and A. Delabie, *J. Phys. Chem. C* **124**, 7163 (2020).
- <sup>48</sup>M. J. M. Merckx *et al.*, *J. Phys. Chem. C* **126**, 4845 (2022).
- <sup>49</sup>T. E. Sandoval and S. F. Bent, *J. Phys. Chem. C* **121**, 25978 (2017).
- <sup>50</sup>B. Shong, R. Y. Brogaard, T. E. Sandoval, and S. F. Bent, *J. Phys. Chem. C* **118**, 23811 (2014).
- <sup>51</sup>T. E. Sandoval and S. F. Bent, *Langmuir* **33**, 8716 (2017).
- <sup>52</sup>K. T. Wong, S. N. Chopra, and S. F. Bent, *J. Phys. Chem. C* **116**, 12670 (2012).
- <sup>53</sup>J. W. Evans, *Rev. Mod. Phys.* **65**, 1281 (1993).
- <sup>54</sup>E. L. Hinrichsen, J. Feder, and T. Jossang, *J. Stat. Phys.* **44**, 793 (1986).
- <sup>55</sup>J. Feder, *J. Theor. Biol.* **87**, 237 (1980).
- <sup>56</sup>J. Talbot, G. Tarjus, P. R. Van Tassel, and P. Viot, *Colloids Surf. A* **165**, 287 (2000).
- <sup>57</sup>M. Schmidt, *J. Phys.: Condens. Matter* **14**, 12119 (2002).
- <sup>58</sup>P. M. Pasinetti, L. S. Ramirez, P. M. Centres, A. J. Ramirez-Pastor, and G. A. Cwilich, *Phys. Rev. E* **100**, 1 (2019).
- <sup>59</sup>N. I. Lebovka, N. V. Vygoritskii, and Y. Y. Tarasevich, *Phys. Rev. E* **102**, 22133 (2020).
- <sup>60</sup>R. H. Swendsen, *Phys. Rev. A* **24**, 504 (1981).
- <sup>61</sup>A. Cadihne, N. A. M. Araújo, and V. Privman, *J. Phys.: Condens. Matter* **19**, 065124 (2007).
- <sup>62</sup>L. Budinski-Petković, I. Lončarević, Z. M. Jakšić, and S. B. Vrhovac, *J. Stat. Mech.: Theory Exp.* **2016**, 053101 (2016).
- <sup>63</sup>G. Mazaleyrat, A. Estève, L. Jeloica, and M. Djafari-Rouhani, *Comput. Mater. Sci.* **33**, 74 (2005).
- <sup>64</sup>A. Estève, Y. J. Chabal, K. Raghavachari, M. K. Weldon, K. T. Queeney, and M. Djafari Rouhani, *J. Appl. Phys.* **90**, 6000 (2001).
- <sup>65</sup>S. B. S. Heil, J. L. van Hemmen, C. J. Hodson, N. Singh, J. H. Klootwijk, F. Roozeboom, M. C. M. van de Sanden, and W. M. M. Kessels, *J. Vac. Sci. Technol. A* **25**, 1357 (2007).
- <sup>66</sup>G. Dingemans, C. A. A. van Helvoirt, D. Pierreux, W. Keuning, and W. M. M. Kessels, *J. Electrochem. Soc.* **159**, H277 (2012).
- <sup>67</sup>G. Kresse, *J. Non-Cryst. Solids* **192–193**, 222 (1995).
- <sup>68</sup>G. Kresse and J. Furthmüller, *Comput. Mater. Sci.* **6**, 15 (1996).
- <sup>69</sup>G. Kresse and J. Hafner, *Phys. Rev. B* **49**, 14251 (1994).
- <sup>70</sup>G. Kresse and J. Furthmüller, *Phys. Rev. B* **54**, 11169 (1996).
- <sup>71</sup>Software: MedeA version 2.23, MedeA and Materials Design are registered trademarks of Materials Design, Inc., Angel Fire: New Mexico (2019).
- <sup>72</sup>J. P. Perdew, K. Burke, and M. Ernzerhof, *Phys. Rev. Lett.* **77**, 3865 (1996).
- <sup>73</sup>S. Grimme, J. Antony, S. Ehrlich, and H. Krieg, *J. Chem. Phys.* **132**, 154104 (2010).
- <sup>74</sup>S. Grimme, *J. Comput. Chem.* **27**, 1787 (2006).
- <sup>75</sup>P. E. Blöchl, *Phys. Rev. B* **50**, 17953 (1994).
- <sup>76</sup>H. J. Monkhorst and J. D. Pack, *Phys. Rev. B* **13**, 5188 (1976).
- <sup>77</sup>R. Chen and S. F. Bent, *Chem. Mater.* **18**, 3733 (2006).
- <sup>78</sup>J. E. Lennard-Jones, *Proc. Phys. Soc.* **43**, 461 (1931).
- <sup>79</sup>M. Hu, T. C. Hauger, B. C. Olsen, E. J. Luber, and J. M. Buriak, *J. Phys. Chem. C* **122**, 13803 (2018).
- <sup>80</sup>I. Levin and D. Brandon, *J. Am. Ceram. Soc.* **81**, 1995 (1998).
- <sup>81</sup>T. Suzuki, S. Hishita, K. Oyoshi, and R. Souda, *Surf. Sci.* **437**, 289 (1999).
- <sup>82</sup>A. Dalton, D. Llera-Hurlburt, and E. Seebauer, *Surf. Sci.* **494**, L761 (2001).
- <sup>83</sup>J. Barth, *Surf. Sci. Rep.* **40**, 75 (2000).
- <sup>84</sup>J. Weckesser, J. V. Barth, and K. Kern, *J. Chem. Phys.* **110**, 5351 (1999).
- <sup>85</sup>A. Kouchi, K. Furuya, T. Hama, T. Chigai, T. Kozasa, and N. Watanabe, *Astrophys. J. Lett.* **891**, L22 (2020).
- <sup>86</sup>D. A. Arthur, D. L. Meixner, M. Boudart, and S. M. George, *J. Chem. Phys.* **95**, 8521 (1991).
- <sup>87</sup>B. Han *et al.*, *J. Phys. Chem. C* **116**, 947 (2012).
- <sup>88</sup>K. Lee and Y. Shim, *RSC Adv.* **10**, 16584 (2020).
- <sup>89</sup>G.-Y. Fang, L.-N. Xu, Y.-Q. Cao, L.-G. Wang, D. Wu, and A.-D. Li, *Chem. Commun.* **51**, 1341 (2015).



<sup>90</sup>M. L. O'Neill, H. R. Bowen, A. Derecskei-Kovacs, K. S. Cuthill, B. Han, and M. Xiao, *Interf. Mag.* **20**, 33 (2011).

<sup>91</sup>M. A. Mione, V. Vandalon, A. Mameli, W. M. M. Kessels, and F. Roozeboom, *J. Phys. Chem. C* **125**, 24945 (2021).

<sup>92</sup>K. V. Wagaskar, R. Late, A. G. Banpurkar, A. V. Limaye, and P. B. Shelke, *J. Stat. Phys.* **181**, 2191 (2020).

<sup>93</sup>See supplementary material at <https://www.scitation.org/doi/suppl/10.1116/6.0002096> for additional DFT results and the IR spectra showing ethanol displacement.